Microporous and Mesoporous Materials 330 (2022) 111604

Contents lists available at ScienceDirect

Microporous and Mesoporous Materials

journal homepage: www.elsevier.com/locate/micromeso

Hierarchical porous fluorine-doped silicon oxycarbide derived materials: Physicochemical characterization and electrochemical behaviour

M. Alejandra Mazo *, Maria T. Colomer, Aitana Tamayo, Juan Rubio

Instituto de Cerámica y Vidrio (CSIC), C/ Kelsen 5, 28049, Madrid, Spain

ARTICLE INFO

Keywords:
Hierarchical porous materials
Micro-meso-macroporous materials
HF etching
F-doped silicon oxycarbide
Supercapacitor

ABSTRACT

Novel hierarchical micro-meso-macroporous fluorine-doped silicon oxycarbide derived materials have been obtained by HF etching of silicon oxycarbides pyrolyzed at different temperatures. The influence of etching time (1 or 24 h) and pyrolysis temperature (from 1100 to 1400 °C) on the selective removal of the silica nano-domains present in the silicon oxycarbide and the appearance of oxygen and fluorine functionalities have been determined and evaluated in terms of their electrochemical response. The insertion of fluorine in the silicon oxycarbide matrix (Si–O(F) bonds) and free carbon phase (C–F semi-ionic and C–F covalent bonds) was corroborated. The materials pyrolyzed at 1300–1400 °C and etched during 24 h show values of specific capacitance as high as 225-165 Fg^{-1} (0.1–30 Ag^{-1}) using a symmetrical configuration and H_2SO_4 1 M as electrolyte. These materials displayed energy density values of 28-19 $Whkg^{-1}$ (0.1–45 $kWkg^{-1}$). The hierarchical microstructure in conjunction with the oxygen and fluorine functionalities are essential in order to explain their good electrochemical response. In particular, those materials present the highest amount of meso (3–10 nm) and larger meso-macropores and the highest content of fluorine in their composition. Then, fluorine-doped silicon oxycarbide derived materials can be potentially used as electrodes for supercapacitors in the field of energy storage applications.

1. Introduction

Nowadays porous silicon oxycarbide (SiOC), silicon oxycarbide derived carbon (SiOC-DC) and carbide derived carbon materials (C-DC) have been gained an increasing attention due to their potential application for energy applications such as gas storage (H_2 and CH_4) [1,2], CO_2 capture [3,4], electrodes for metal ion batteries (Li, [5,6] Na [6,7], and Zr [8]) and supercapacitors [9,10]. In addition, an increasing interest has been focused for supercapacitors applications, also known as electrical double layer capacitors (EDLCs), due to their higher power density (P_d), long cycle life, fast charge-discharge rate, low cost and satisfactory safety [11,12]. The main requirements in order to achieve a good capacitance response are high electrical conductivity and tuned porosity. In this sense, a high electrical conductivity can be easily obtained in those materials increasing the amount of carbon and/or increasing the pyrolysis temperature [13]. However, the fabrication of a suitable porous microstructure in order to enhance its electrochemical response is not an easy task and many efforts have been recently done [10,11,14,15]. Microporous carbon derived materials with very high specific surface area (SSA, 2000–3000 m^2g^{-1}) due to their small pore size display moderate specific capacitance (C_s) values and a poor rate performance [15]. Micropores with too small size lead to a poor wettability of the electrolyte reducing both the ion accessibility and the diffusion rate [12].

The development of hierarchical porous materials, with micro, meso and also macropores up to an adequate value, enhances the ion accessibility and mass diffusion pathways and hence, the C_s and energy density (E_d) values of the related carbon derived materials [10,11,14,15]. The functionalization of the porous carbon surface with O or N-containing groups increases the wettability and induces the formation of Faradaic reactions of the carbon materials increasing the electrochemical response [14–16]. Another functionalization of the carbon materials (*i.e.,* graphite, graphene, graphene oxide (GO)) less explored which also enhances the electrochemical properties can be performed by fluorine. The presence of C–F semi-ionic bonds increases the ion transport, enhances the electrical conductivity and provides sites for Faradaic reactions [17]. Finally, the type of electrolyte employed deeply influences the electrochemical performance of the designed

* Corresponding author.
E-mail address: sandra@icv.csic.es (M.A. Mazo).

https://doi.org/10.1016/j.micromeso.2021.111604
Received 21 October 2021; Received in revised form 25 November 2021; Accepted 28 November 2021
Available online 30 November 2021

supercapacitor [18].

There are several strategies to develop porous materials, [19,20] some of them have been employed to produce porous SiOC-DC and C-DC for supercapacitor applications. During the last decades extremely high porous materials with a great contribution of microporous were basically obtained by chlorine etching of SiOC or carbide materials [9, 21–23]. If chlorine etching is used, the extraction of SiC but also SiO_2 phase generates hierarchical porous carbonaceous materials with elevated *SSA* (associated to a great amount of micropores) and pore volume, but small and narrow pore diameters. The yield of the pyrolysis and Cl_2 etching processes is very low, being this fact very relevant for the economic viability of this method to be industrially used in the production of porous materials. Nowadays, the need of the development of more sophisticated hierarchically carbonaceous porous derived materials with micro, meso and also macropores have done that other etching procedures, performed with HF [24–27] or alkaline hydroxides (i.e. NaOH) [10,11,28,29], have gained importance. The HF etching removes at R.T. the silica nano-domains present in the SiOC material, while in the case of alkaline hydroxides medium temperatures (above 400 °C) are required to remove silica and also high temperatures (750–800 °C) are used to the activation of C necessary for a good electrochemical response [10]. HF and alkaline hydroxide etching occurs via the nucleophilic attack of F^- or OH^- ions which leads to the breakage of highly polarized Si–O–Si bonds [30]. In the case of SiOC materials pyrolyzed at low temperatures (< 1200 °C), the presence of a mixed network of Si–O–C hinders this attack and in fact, less polarized Si–C bonds are not etched [31]. As the pyrolysis temperature increases (above 1200 °C), SiOC undergoes the phase separation (into SiO_2, SiC and C) and silica can be easily removed and a higher porosity is developed [32]. Here, we propose the use of HF etching instead of using alkaline hydroxides since the latter etching requires higher temperatures therefore, a priori the HF etching that needs lower temperatures is a softer, more sustainable and environmentally friendly approach.

Apart of the etching procedure, there are other parameters that can be adjusted such as the initial precursors, synthesis conditions, pyrolysis temperature, the final shape of the materials as powder or bulk, etc., [24, 27,32,33] that will determine the final porous carbon derived material characteristics and hence their potential uses. The presence of Si–H functionalities in the hybrid enhances the insertion of C within the silica network in the resulting SiOC after pyrolysis [34]. Furthermore, the presence of Si-Ph functionalities in the silicon precursors increases the amount of C_{free} in the final carbon enriched SiOC [35] and therefore, their electrical conductivity [13]. In a previous work [27], we developed novel trietoxysilane/dimethyldiphenylsiloxane (TREOS/DMDPS) hybrids with Si–H and Si-Ph functionalities that after pyrolysis (from 1100 to 1400 °C) and HF etching (HF 40%, 5 h) gave as a result hierarchical micro-mesoporous SiOC-DC materials. Generally, the experimental etching conditions employed are: diluted HF solutions (20%), medium times (6–9 h) and powder SiOC samples [20,25,26,32,36]. In addition, it is important to note that HF etching time is a parameter rarely studied in the literature [37,38]. *Wilson* et al. [38] studied the influence of etching time from 15 min to 24 h and *Soraru* et al. [37] from 0 to 2 h. However, it is necessary to study the influence of HF in the removal of the silica nano-domains during etching. Taking into account the lack of information in this regard, the aim of this work is to determine the role of HF in the SiO_2 removal and the impact of etching time -employing very short or long times (1 or 24 h)- on the structure and microstructure of TREOS/DMDPS SiOC derived materials pyrolyzed at different temperatures (from 1100 to 1400 °C). In addition, the effect of etching time on the electrochemical performance of the resulting materials was also studied. Then the relationships between composition, microstructure and electrochemical response of those hierarchical porous F-doped SiOC-DC materials and their potential use as electrodes for supercapacitor applications have been studied.

2. Experimental section

2.1. Materials preparation

The sol-gel hybrid was synthesized employing TREOS ($(SiH(OCH_2CH_3)_3$; 97% (ABCR, Germany)) and DMDPS silanol terminated $(OH–Si(CH_3)_2–O-[Si(CH_3)_2–O]_n[Si(C_6H_5)_2–O]_m-Si(CH_3)_2OH$; average molecular weight of 900–1000 g mol^{-1} (ABCR, Germany)). The TREOS/DMDPS weight ratio was 60/40 and the molar ratio of isopropanol (i-PrOH, for analysis (Merck, Germany)), water and hydrochloric acid (HCl, 37%, for analysis (Merck, Germany)) were TREOS/i-PrOH/H_2O/HCl = 1/6/3/0.01. The SiOCs were obtained by pyrolysis under flowing N_2 in the temperature range from 1100 to 1400 °C, with a heating/cooling rate of 5 °C.min^{-1} and a dwelling time of 1 h. The SiOCs were grounded employing an agate mortar and then the powders were sieved below 200 μm (N70 ASTM Standard). Subsequently, the etching was performed with 1 g of SiOC powders and 50 cm^3 of HF (40% wt./wt., for analysis (Scharlab, Germany)), the mixture was placed into a polypropylene container and continuously stirred at R.T. during 1 or 24 h. After that, the powders were filtered and rinsed with H_2O several times to remove any residual HF and dried at 50 and 100 °C during at least 48 h. Futher experimental details can be found elsewere [27].

The samples were denoted as TRP (for the hybrid material), TRPxx (for SiOC materials) or TRPxxFyy (for SiOC-DC materials), where TR corresponds to TREOS, P to DPDMS, xx indicates the pyrolysis temperature (11 = 1100 °C, 12 = 1200 °C, 13 = 1300 °C and 14 = 1400 °C, respectively) and finally, Fyy the etching time (F1 = 1 h and F24 = 24 h, respectively).

2.2. Materials characterization

The C (%) and O (%) contents were determined by the elemental analyzers CS-200 and TC-500 (Leco Corp., USA) and the Si(%) was calculated by difference from 100%. The SiOC formula ($SiOC_xO_{2(1-x)}$ + C_{free}) was rewritten as xSiC + (1-x) SiO_2 + C_{free} considering that all the C atoms present in SiOC material can progress to form SiC [39]. The % volume of SiC, SiO_2 and C was calculated in accordance with [27]. The structure evolution from SiOC to SiOC-DC was followed by means of Fourier Transform Infrared spectroscopy (FT-IR) employing a Spectrum BX (PerkinElmer Corp., USA) with a resolution of 4 cm^{-1} and, X-ray diffraction (XRD) analysis which was conducted using a D8 Advance (Bruker, USA) apparatus employing a Cu kα radiation (λ = 0.154178 nm) in the range of $10 \leq 2\Theta \leq 90°$ by steps of 0.05° and acquisition time of 1.5 s per step. The surface elemental analysis was evaluated by X-ray photoelectron spectroscopy (XPS, PHOIBOS 150 9MCD spectrometer, SPECS GmbH, Germany) in the constant analyzer energy mode with a non-monochromatic Mg X-ray source (1253.6 eV, 200 W and 12 kV) for SiOC and SiOC-DC powder samples mounted over a Cu foil tape. A survey and high resolution spectra were run for each sample, setting the pass energy at 50 and 20 eV, respectively and a raster area of 5 × 5 mm^2. Peak positions were calibrated to 284.6 eV employing C1s spectrum. Data analysis was done employing CASA XPS software with a *Shirley* background subtraction. The peak fitting was performed by using a non-linear least-squares method adopting *Gaussian–Lorentzian* peak shapes. Raman spectra were obtained from an InVia Raman spectrometer (Renishaw plc., UK) equiped with a 514 nm Ar^+ laser and calibrated with the 520 cm^{-1} band of the metallic Si. N_2 adsorption–desorption experiments were carried out at −192 °C using a Tristar 3000 (Micromeritics Corp., USA). *SSA* was evaluated by *Brunauer-Emmet-Teller* equation (BET) [40], employing the adsorption data in the p/p^o range from 0.05 to 0.20. The pore size distribution (PSD) in the mesoporous range (2–50 nm), surface area of mesopores (S_{meso}), volume of mesopores (V_{meso}) and mesopore diameter (D_{meso}) were obtained from the adsorption branch of the isotherm using the *Barrett-Joyner-Halenda* equation (BJH) [41]. To evaluate the microporosity (< 2 nm) the surface area of micropores (S_{micro}) was calculated subtracting S_{meso} from the SSA

calculated from BET. Micropore volume (V_{micro}) was calculated subtracting V_{meso} from the total volume measured by the single point at $p/p^o = 0.99$. The microstructure of the materials was studied with field emission scanning electron microscopy (FE-SEM, Hitachi S-4700, Japan).

2.3. Electrochemical characterization

The electrochemical measurements of the SiOC-DC materials were carried out using a symmetrical (*i.e.,* two electrodes) cell configuration containing 1 M H_2SO_4 solutions as electrolyte. For the working electrode approximately 5 mg of active material (SiOC-DC) was mixed in an agate mortar with carbon black as a conductive agent (CB, EnsacoTM E250G, Timcal, Imerys Graphite & Carbon, USA; $SSA_{CB} = 43\ m^2g^{-1}$) and polytetrafluoroethylene as a binder agent (PTFE, Aldrich, USA), with a weight ratio (70:10:20). After that, few drops of N-methyl-2-pyrrolidinone (Aldrich, USA) were added and a black slurry was formed. Then, the working electrode was prepared by direct deposition over the stainless steel current collectors which during the assembly were separated by a porous membrane (MF- Milipore mixed cellulose ester). After that, the slurry was dried at 70 °C for 48 h and then soaked with the electrolyte for at least 48 h. Cyclic voltammetry (CV), electrochemical impedance spectroscopy (EIS) and galvanostatic charge and discharge (GCD) experiments were carried out on a PGSTAT204 potentiostat/galvanostat (Metrohm Autolab, B.V., Switzerland) electrochemical analyser. CV was performed at a potential range from −0.3 to +0.6 V. Different scan rates ranged from 10 to 1000 mVs^{-1} were studied. EIS measurements were analysed from 0.01 to 10^5 Hz. GCD experiments were performed employing cut offs with the same potential window of CV experiments at increasing current densities up to 30 Ag^{-1}. The C_s of the samples were calculated from the galvanostatic discharge (GD) curves using (1) [42],

$$C_s\ (Fg^{-1}) = 4It_d/m\Delta V \quad (1)$$

Where 4 is a coefficient related to full cell configuration (two electrodes), I(A) is the current used to discharge the system, t_d (s) is the discharge time, m (g) is the average of both carbon electrodes considering only the active mass material (SiOC-DC) and ΔV (V) is the potential range of the discharge. The E_d of the electrode material was calculated from (2).

$$E_d\ (Whkg^{-1}) = C_s\ V^2/2 \times 1000\ (g/kg)\ x\ 1/3600\ (WhJ^{-1}) \quad (2)$$

Where C_s is the specific capacitance (Fg^{-1}) and V (V) is the operating voltage. The P_d of the electrode was calculated from (3) by dividing the E_d by t_d at certain current densities.

$$P_d\ (kWkg^{-1}) = E_d/t_d\ x\ 3600\ (s/h)\ x\ 1/1000\ (W/kW) \quad (3)$$

3. Results and discussion

3.1. Evolution of composition and structure of the porous materials

The influence of etching time, 1 or 24 h, has been analysed by the evolution of the composition of the silica and carbon phases (*i.e.,* SiC and C) for carbon enriched SiOC materials pyrolyzed from 1100 to 1400 °C by means of chemical analysis, FT-IR, XRD and XPS.

After HF etching during 1 or 24 h, the evolution of the composition for SiOC-DC materials is collected in Table 1. The initial SiOC materials display a high C(%) (≈ 26%) value for all the pyrolysis temperatures [27]. For the samples etched during 1 h the C(%) value steadily increases from 1100 °C to higher pyrolysis temperatures (TRP11F1 C(%) = 29.2 to TRP14F1 C(%) = 53.1, Table 1). In contrast, for the etching time of 24 h, the C(%) value is very high and fairly similar independently of the pyrolysis temperature (TRP11F24 C(%) = 51.8 to TRP14F24 C(%) = 53.5,

Table 1
Evolution of the composition during HF etching time of 1 or 24 h of TREOS/PDMDP hybrids pyrolyzed from 1100 to 1400 °C.

	C (%)	O (%)	Si (%)	Formula	SiO_2 (%)	SiC (%)	C (%)
TRP11F1	29.2	31.5	39.3	$SiC_{1.74}O_{1.41}$	62	13	25
TRP12F1	46.5	20.6	32.9	$SiC_{3.31}O_{1.10}$	41	16	43
TRP13F1	53.2	16.6	30.3	$SiC_{4.11}O_{0.96}$	33	17	49
TRP14F1	53.1	15.3	31.6	$SiC_{3.92}O_{0.85}$	31	20	49
TRP11F24	51.8	25.0	23.2	$SiC_{5.21}O_{1.88}$	47	2	51
TRP12F24	52.0	17.9	30.1	$SiC_{4.04}O_{1.04}$	36	16	48
TRP13F24	53.9	15.8	30.3	$SiC_{4.15}O_{0.91}$	32	18	50
TRP14F24	53.5	14.4	32.0	$SiC_{3.90}O_{0.79}$	29	22	49

Table 1). The results in Table 1 indicate that for the shortest etching time (1 h) the removal of silica nano-domains is favoured with the phase separation of SiOC as the pyrolysis temperature increases. SiO_2 (%) halves, SiC (%) slightly increases and C(%) doubles when the pyrolysis temperature varies from 1100 to 1400 °C (Table 1). However, for the longest etching time the initial hindrance of the SiOC phase, which prevents Si–O bonds for breakage [31], is supplied with the increase of etching time up to 24 h and therefore, the evolution of composition is totally different; SiO_2 (%) progressively decreases, SiC (%) sharply increases and C(%) remains high and fairly constant as the pyrolysis temperature increases (Table 1). The biggest compositional differences have been found between the samples pyrolyzed at 1100 °C. TRP11F1 is composed by 62/13/25 of SiO_2/SiC/C and TRP11F24 by 47/2/51. These differences could be determinant for the electrochemical response of the resulting SiOC-DC materials.

As it occurs for the chemical composition data (Table 1), there are great differences between the FT-IR spectra of the SiOC-CD samples etched during 1 or 24 h (Fig. 1 (a) and (b), respectively). As it was previously observed, as the pyrolysis temperature increases the SiOCs are more phase separated and the nucleophilic attack of HF is more favoured. This fact is especially observed between the samples pyrolyzed at 1100 °C and higher temperatures [24,27]. The increase of the pyrolysis temperature promotes the phase separation of SiOC into SiO_2 and SiC, but also the reorganization and the incipient crystallization of SiC and C_{free} phases, making easier the SiO_2 extraction by HF. A similar trend is appreciated as the etching time increases. As a result, as the HF etching attack is greater (*i.e.,* higher pyrolysis temperature and etching time) the bands related to SiO_2 (1080 cm^{-1} (Si–O–Si asymmetric stretching), 810-800 cm^{-1} (Si–O–Si symmetric stretching) and 460 cm^{-1} (O–Si–O bending vibration modes)) [43] of SiOC material are drastically reduced due to the selective removal of silica nano-domains. In addition, the IR bands that belong to SiC (≈ 850 cm^{-1} contribution of amorphous a-SiC = 880 cm^{-1} and β-SiC = 792 cm^{-1} Si–C stretching) [44,45] and C_{free} (≈ 1580 cm^{-1} C═C stretching) [46] are enhanced. It is important to note that in the case of the samples pyrolyzed at temperatures ≥1200 °C a band located at ≈ 950 cm^{-1}, related to the presence of silanol groups and/or S–F bonds created as a consequence of the HF attack over Si–O bridged bonds [47,48], is clearly displayed. Other new bands also appear around 1700, 1630, 1230 and 1150 cm^{-1} in the samples pyrolyzed ≥1200 °C and etched during 1 h. The band at 1630 cm^{-1} comes from the adsorbed H_2O over the surface of the porous samples. More interesting are the bands located at ≈ 1700 and ≈ 1230 cm^{-1} associated to C═O functionalities (≈ 1700 cm^{-1} (C═O stretching) and ≈ 1230 cm^{-1}(C–O stretching), respectively). Additionally, the bands located at 1230 and 1150 cm^{-1} can be assigned to C–F bonds with covalent or semi-ionic character, [49] indicating the grafting of fluorine into the graphene layers of the C_{free} phase. Those bands are more intense in the case of the samples etched during 24 h appearing for all the pyrolysis temperatures (Fig. 1 (b)). The presence of O functionalities (*i.e.,* C═O) has been previously reported for SiOC etched with HF [46,47]. Their formation can be explained by the oxidation as a consequence of the HF attack over Si–O bridged bonds with the contribution of the C_{free}

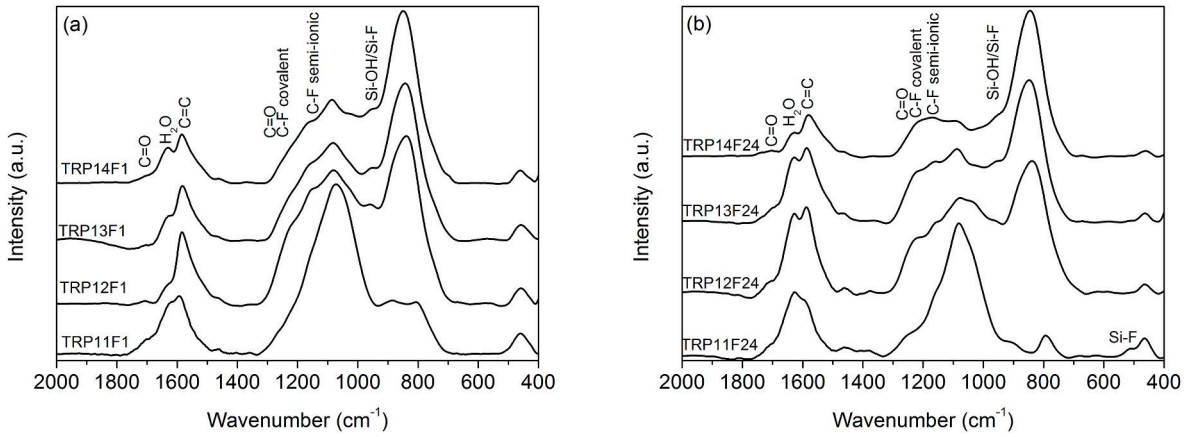

Fig. 1. FT-IR spectra of TRF SiOC-CD materials etched during (a) 1 or (b) 24 h at different pyrolysis temperatures.

phase [47]. Finally, in the case of the sample pyrolyzed at 1100 °C and etched during 24 h a band related to Si–F bonds (510 cm^{-1} Si–F stretching) [50] appears, showing the plausible insertion of fluorine within the SiOC network as it will be corroborated below by XPS. In accordance with Table 1, it is also observed a very low contribution of the SiC bonds (890 cm^{-1}) which may indicate the replacement of C by F.

Fig. 2 (a) and (b) display the XRD patterns of SiOC-DC after HF etching during 1 or 24 h, respectively. For the etching time of 1 h (Fig. 2 (a)), the XRD patterns of SiOC-DC are rather similar of pristine TRP SiOC materials [27] but a slightly increase of the peaks related to SiC and C is appreciated due to the removal of silica nano-domains. At 1100 °C the material is featureless, but as the pyrolysis temperature increases, the phase separation and rearrangement of the SiOC material reveal both the SiO_2 and C phases (SiC and C_{free}) which present an incipient crystallization. SiO_2 appears as a broad halo at $2\Theta \approx 22°$ and SiC displays the strongest peaks located at $2\Theta \approx 35$, 60 and 75 ° ((111), (220) and (311) lattice planes, respectively, JCP: 00- 029–1129). C_{free} shows medium intensity peaks located at $2\Theta \approx 27$, 43–44 ° ((002), (10) lattice planes (JCP: 00-041-1487)) related to ordered and disordered carbon structures, respectively [45]. It is important to note that the main bands of SiO_2 and C appear overlapped ($2\Theta \approx 25°$) as a broad halo. However, as the silica extraction is larger the peak upshifts making the C peak more evident, being especially noticeable for TRP13F1 and TRP14F1 samples.

In the case of 24 h of etching time (Fig. 2 (b)), the favoring of the intensity of the C bands is higher as a result of a major extraction of silica nano-domains. In any case and in accordance with compositional (Table 1) and FT-IR results (Fig. 1 (b)), the SiO_2 peak is always appreciated indicating that the SiO_2 phase is not totally removed in any case. Finally, in the case of the TRP11F24 sample the presence of fluorinated-graphite like structures with a sharp peak located at $2\Theta \approx 18°$, associated to C–F bonds of F-intercalated graphite, is mainly observed [51]. Similar results were previously reported for SiOC-DC materials etching with HF [46]. This peak can be scarcely appreciated in other samples. The HF etching times and high concentration of HF (*i.e.,* 40%) could produce the insertion of fluorine into both, the matrix and C_{free} generating Si–F and C–F bonds detected by FT-IR (Fig. 1) and XRD (Fig. 2), respectively. The influence of these bonds into the electrochemical response will be determinant and commented later.

In order to corroborate the appearance of fluorine and/or O-containing functionalities after HF etching, XPS measurements were also performed over pristine SiOC (i.e. TRP11) and SiOC-CD (i.e. TRP11F1 and TRP1124) samples. The survey spectra are collected in Fig. 3 (a) and Table 2. The high resolution spectra of F1s, C1s, Si2p and O1s are collected in Fig. 3 (b)–(d), Figure SI1(a)–(d), Figure SI2(a)–(d) and Figure SI3(a)-(b), respectively. The high resolution spectra of each sample have been decomposed into the main components and the binding energy values (BE) and percentage of each component are summarized in Table 3.

The XPS survey spectrum of the TRP11 sample shows that the SiOC is composed only of Si, O and C displaying the O1s, C1s, Si2s, Si2p and O2s core bands and besides some *Auger* bands. The SiOC-DC samples also contain the bands related to F1s and related *Auger* bands, which corroborate the presence of the fluorine insertion in accordance with FT-IR (Fig. 1) and XRD results (Fig. 2). The surface composition of the studied samples is collected in Table 2 and only has been taken into account to confirm the presence of F due to the local and surface characteristic of the XPS analysis. As it is expected, as etching time increases the C(%) increases from SiOC to SiOC-DC in accordance with the

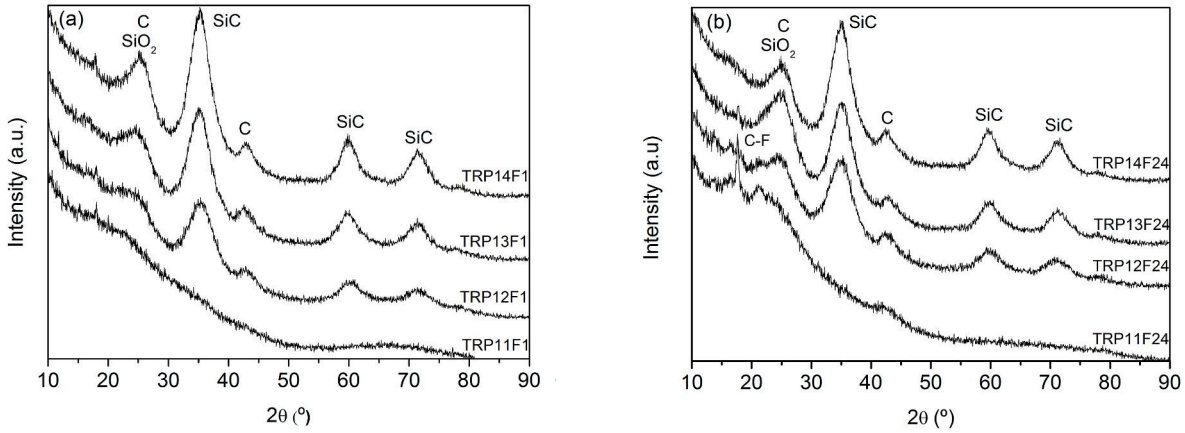

Fig. 2. XRD patterns of SiOC-DC etched during (a) 1 or (b) 24 h at different pyrolysis temperatures.

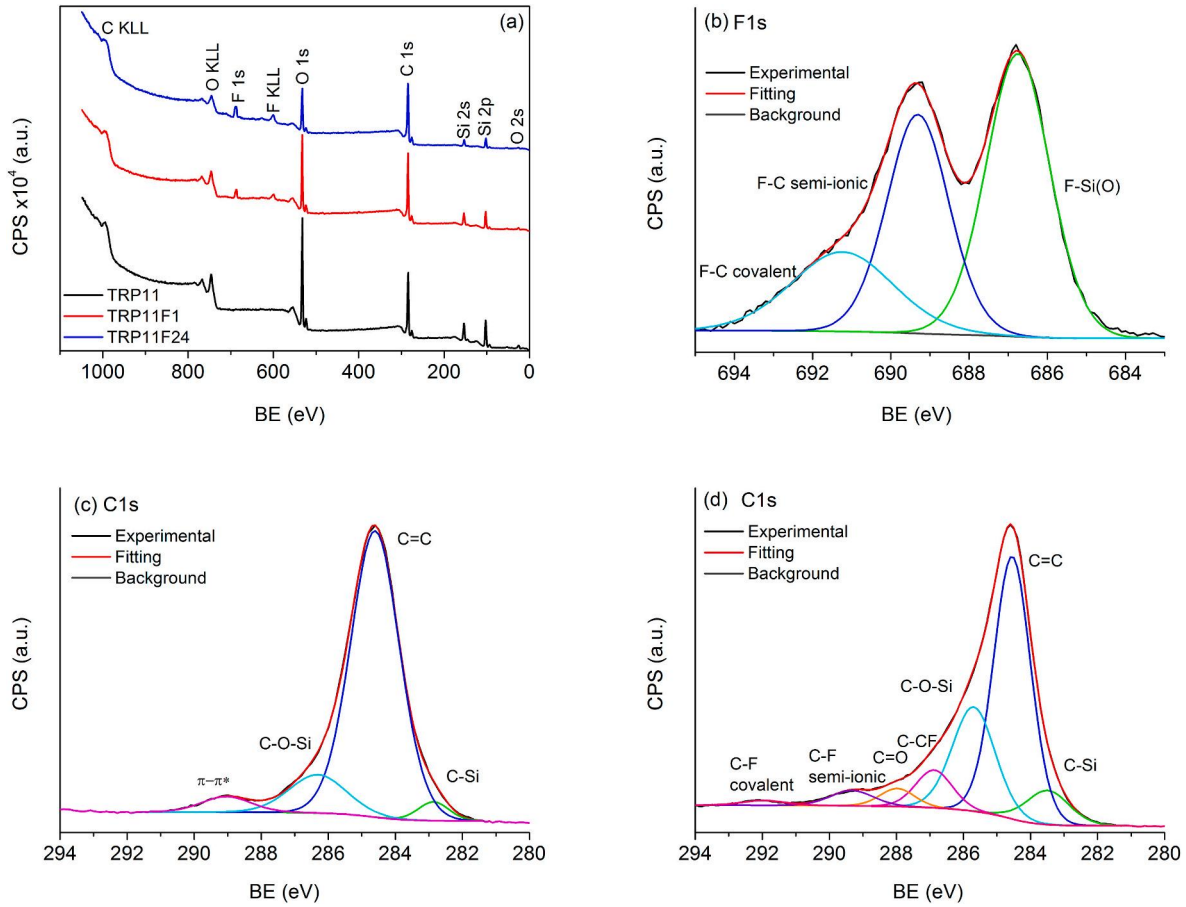

Fig. 3. (a) Survey XPS spectra of TRP11, TRP11F1 and TRP11F24 samples. High resolution XPS spectra (b) of F1s for TRP11F24, (c) of C1s for TRP11 and (d) of C1s for TRP11F24, respectively.

Table 2
XPS surface composition of TRP11, TRP11F1 and TRP11F24 samples.

	C (%)	Si (%)	O (%)	F (%)
TRP11	33.9	36.2	29.8	–
TRP11F1	41.6	28.7	25.5	4.1
TRP11F24	52.3	18.7	20.5	8.5

chemical composition obtained from Table 1. More important is the existence of F in SiOC-DC materials. Its value concentration increases with etching time from 4.1 to 8.5% (Table 2).

In the case of TRP11 sample, the O1s spectrum (Figure SI1(a) can be decomposed into three components assigned to SiO_2 (533.73 eV), Si–O–Si (532.43 eV) and SiO/Si–OH (530.39 eV), respectively, [31,52,53] being Si–O–Si the one with the highest intensity (Table 3). The Si2p spectrum can be decomposed into three components assigned to SiO_4 (103.60 eV), SiO_3C (102.90 eV) and SiO_2C_2 (101, 27 eV) [54], respectively, being SiO_3C the main component of the SiOC phase (Table 3). Finally, the C1s spectrum can be decomposed into four components assigned to C–Si (282.86 eV), C═C (Csp^2) (284.60 eV), C–O–Si (SiOC) bonds (286.30 eV) [54], and the characteristic shake-up satellite peak of aromatic carbons involving the energy of $\pi \rightarrow \pi^*$ transition (289.00 eV) [53], respectively. The main component is the one related to the C_{free} phase (Table 3).

The SiOC-CD materials display the F1s spectra which can be decomposed into three components related to F–Si and F–C bonds. The first component at ≈ 687 eV can be tentatively assigned to F–Si bonds with the participation of oxygen (SiF(O)) [48,52] and it is related to F-doped SiOC matrix. The other two components are located at ≈ 689 and ≈ 692 eV and correspond to F–C bonds with semi-ionic or covalent character, respectively [17,55]. Both are related to F-doped C_{free} phase (Table 3). This assumption perfectly agrees with FT-IR (Fig. 1) and XRD

Table 3
BE values and content in percentage (in parenthesis) of O1s, Si2p, C1s and F1s for TRP11, TRP11F1 and TRP11F24 samples obtained from the XPS high resolution spectra.

Sample	TRP11	TRP11F1	TRP11F24
O1s			
SiO/SiOH	530.39 (1.7%)	530.61 (1.7%)	530.13 (1.8%)
Si–O–Si	532.43 (85.8%)	532.51 (83.1%)	532.51 (82.9%)
SiO_2	533.73 (12.4%)	533.81 (14.0%)	534.06 (13.9%)
C=O	–	535.45 (1.1%)	536.18 (1.4%)
Si2p			
SiO_2C_2	101.27 (19.2%)	101.37 (21.9%)	101.43 (29.2%)
SiO_3C	102.90 (76.2%)	102.87 (74.6%)	102.52 (66.8%)
SiO_4	103.60 (4.5%)	103.93 (2.4%)	103.92 (1.6%)
SiO(F)	–	105.39 (1.0%)	105.19 (2.3%)
C1s			
C–Si	282.86 (3.3%)	283.33 (8.0%)	283.49 (7.9%)
C=C	284.60 (79.8%)	284.49 (55.1%)	284.54 (52.4%)
C–O–Si	286.30 (12.5%)	285.39 (21.4%)	285.69 (24.2%)
Shake-up C=C	289.00 (4.4%)	–	–
C-CF	–	286.59 (9.7%)	286.88 (7.5%)
C=O	–	287.77 (0.9%)	287.97 (3.4%)
C–F semi-ionic	–	289.08 (4.5%)	289.33 (3.5%)
C–F covalent	–	291.80 (0.48%)	292.00 (1.1%)
F1s			
F–Si(O)	–	686.80 (59.0%)	686.75 (45.4%)
F–C semi-ionic	–	689.20 (37.8%)	689.31 (34.2%)
F–C covalent	–	691.65 (3.1%)	691.24 (20.4%)

(Fig. 2) results. Then, the etching conditions HF 40% and long times produce the incorporation of fluorine, generating F-doped SiOC-CD materials with the insertion of fluorine within both the SiOC matrix and C_{free} phase (*i.e.,* F-doped SiOC and F-doped C_{free}). Apart of the appearance of the F1s peak in the SiOC-CD samples, the HF etching produces important differences in other regions of the XPS spectra (Table 3). The O1s spectra show the presence of a new peak upshifted up to 536.18 eV (≈ 1%) probably due to the presence of C═O bonds as previously was observed by FT-IR (Fig. 1). The Si–O–Si peak slightly decreases as the etching time increases, while the other peaks remain almost similar. The Si2p spectra show the decrease of SiO_3C and SiO_4 units and an increase of the SiO_2C_2 unit due to the evolution of the etching process. The appearance of a new peak upshifted from SiO_4 units (from 103.9 to ≈ 105.2 eV) could be due to SiO(F) units indicating the incorporation of F into the SiOC network. The C1s spectra show the major differences, C–Si and C–O–Si peaks (related to SiOC) increase while C═C peak (related to C_{free}) decreases as the etching time increases. In addition, the appearance of several new peaks related to the presence of O (C═O ≈ 288 eV) and F functionalities (C-CF (≈ 287 eV), C–F semi-ionic (≈ 289 eV) and C–F covalent (≈ 292 eV)) bonds confirm the FT-IR (Fig. 1) and XRD (Fig. 2) results.

The C_{free} phase was further analysed by Raman spectroscopy which is a very powerful technique to characterize carbon materials. The main features of graphite-like structures are the D band (≈ 1350 cm^{-1}), G band (≈ 1580 cm^{-1}) and G′ band (≈ 2700 cm^{-1}). The D band is a breathing mode with A_{1g} symmetry and means disorder [56,57], the G band is a doubly degenerated E_{2g} mode that belongs to Csp^2 bonds and the G' band is related to the D band of the zone-boundary phonons, respectively [56,57]. Their position, width (W), the I_D/I_G ratio and the presence of the second order spectra (i.e. bands located at > 2700 cm^{-1}) are usually employed to analyze the characteristics of carbon materials [56–60]. In this sense, the I_D/I_G ratio is generally used as an indicator of the order degree, a low I_D/I_G ratio means ordering and the reduction of defects [59]. A simple *Lorentz* fitting was performed over Raman spectra of initial SiOCs and SiOC-DCs materials etched with HF (during 1 or 24 h), and the main results are collected in Table 4, Fig. 4 ((a),(b)) and Figure SI4(a),(b).

The SiOC pyrolyzed at 1100 °C displays a C_{free} phase related to highly disordered carbon, with a very broad overlapped D and G bands. As the pyrolysis temperature increases, the C_{free} phase experiences an ordering rearrangement and turns into glassy carbon [60]. The bands become narrower and well-resolved, mainly the D band (WD varies from 140 to 50 cm^{-1}, Table 4), D is upshifted (from 1330 to 1349 cm^{-1}, Table 4) and G downshifted (from 1596 to 1591 cm^{-1}, Table 4), respectively. Finally, the I_D/I_G increases with the pyrolysis temperature (Fig. 4 (b)), according with previous results [43]. The C_{free} phase is embedded within the Si–O–C network which generates high local strains over the graphene layers increasing the disorder as pyrolysis temperature increases [36].

Table 4
Summary of Raman data of SiOC and SiOC-DC pyrolyzed and etched under different conditions. Position and width (Full width at half maximum = W) of D and G bands.

Sample	D (cm^{-1})	WD (cm^{-1})	G (cm^{-1})	WG (cm^{-1})
TRP11	1330	140	1596	65
TRP12	1341	99	1597	59
TRP13	1348	55	1595	55
TRP14	1349	50	1591	59
TRP11F1	1340	137	1594	62
TRP12F1	1342	85	1591	59
TRP13F1	1340	87	1590	58
TRP14F1	1344	61	1589	56
TRP11F24	1343	121	1595	58
TRP12F24	1342	76	1594	56
TRP13F24	1337	89	1596	59
TRP14F24	1340	67	1596	44

After HF etching the Raman spectra display a high luminescence background probably due to the presence of dangling and broken bonds formed during the removing of silica nano-domains, as a result remarkable differences are found for I_D/I_G values (Fig. 4 (b)). In the case of SiOC-DC etched during 1 h, the I_D/I_G values decrease but follow the same trend that pristine SiOC materials (*i.e.,* increasing with the pyrolysis temperature). However, in the samples etched during 24 h the I_D/I_G values are drastically reduced and also are rather similar independently of the pyrolysis temperature. In addition, the G band becomes narrower (from 58 to 44 cm^{-1}, Table 4). After HF etching part of the Si–O–C matrix is removed and the strains are reduced generating a more ordered C_{free} phase. These facts are noticeable with the narrowing of the G band and the decreasing of I_D/I_G values, especially in the samples etched during 24 h [36].

3.2. Microstructural evolution of porous materials during HF etching

Fig. 5 (a) and (c) shows the N_2 adsorption-desorption isotherms, and Fig. 5 (b) and (d) the corresponding PSD of SiOC-DC etched during 1 or 24 h, respectively. Table 5 also collects a summary of the main data. The pristine SiOC materials are non-porous (SSA < 1 m^2g^{-1}), [27] but after the HF etching due to the selective removing of silica nano-domains a highly hierarchical porous microstructure is generated [27]. As it was stated before, in the case of materials pyrolyzed at low temperatures the SiOC mixed network limits the HF attack but as the pyrolysis temperature increases, the phase separation into SiO_2 and SiC favors this attack. Those facts explain the great differences between the samples pyrolyzed at 1100 °C and the others [27]. For the samples etched during 1 h (Fig. 5 (a)), the sample pyrolyzed at 1100 °C (*i.e.,* TRP11F1) displays a type Ib isotherm characteristic of microporous materials [61] with a PSD including wide micropores and narrow mesopores as can be clearly seen in Fig. 5 (b). At higher temperatures (from 1200 to 1400 °C) the volume adsorbed radically increases and the samples display a type IVa isotherm related to the presence of mesopores, but the very fast uptake at low p/p^o also indicates the presence of micropores (≤ 2.5 nm) [61]. The isotherms display a type H4 hysteresis loop related to slit-like pores [61]. At higher temperatures, the phase separation of SiOC makes easier the removal of silica nano-domains increasing the amount of N_2 adsorbed volume but also enlarging the pore diameter as can be seen in Fig. 5 (b), that displays micropores (< 2 nm) and mesopores centered between 3 and 10 nm. In the case of TRP14F1 sample it is worthy to note also the formation of larger pores (*i.e.,* meso-macropores 20–100 nm).

For the longest etching time (24 h, Fig. 5 (c)) the shape of the isotherms is rather similar in all cases except for the uptake at high p/p^o values indicating the presence of macropores. The volume adsorbed is much bigger than the one adsorbed for the sample etched during 1 h, especially for the samples pyrolyzed from 1100 to 1300 °C (Figure SI5). Apart of the presence of micro (< 2 nm) and mesopores (3–10 nm), a greater amount of larger meso-macropores (20–100 nm) is appreciated for all the pyrolysis temperatures (Fig. 5 (d)). In summary, due to the HF etching the SiOC-CD samples are hierarchical highly porous materials composed by micro (< 2 nm), meso (3–10 nm) and also bigger pores, *i.e.,* meso-macropores (≈ 50 nm).

The *SSA* values increase with the pyrolysis temperature reaching a maximum at 1300 °C (Table 5). Independently of the etching time due to the enlargement of the pores after HF attack D_{meso}, S_{meso} and V_{meso} increase up to 1400 °C (Table 5). The parameters of the micropores follow a different behavior, i.e., in the case of samples etched during 1 h those parameters increase up to 1200–1300 °C and then decrease. However, for samples etched during 24 h all the micropore parameters steadily decrease with the pyrolysis temperature (Table 5). It is important to note the great differences between the parameters of the samples pyrolyzed at 1100 °C and etched during 1 or 24 h.

The microstructural characterization has been completed by FE-SEM micrographs (Fig. 6 (a)-(d)). The low magnification FE-SEM images show that the SiOC-DC materials are composed by irregular shape

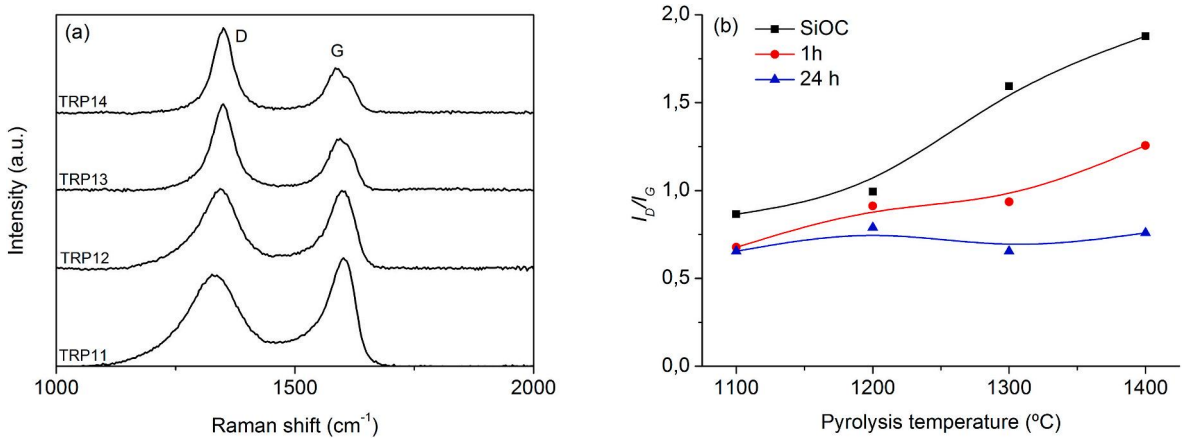

Fig. 4. (a) Raman spectra of TRP SiOC derived materials and (b) I_D/I_G evolution from SiOC to SiOC-DC pyrolyzed and etched under different conditions.

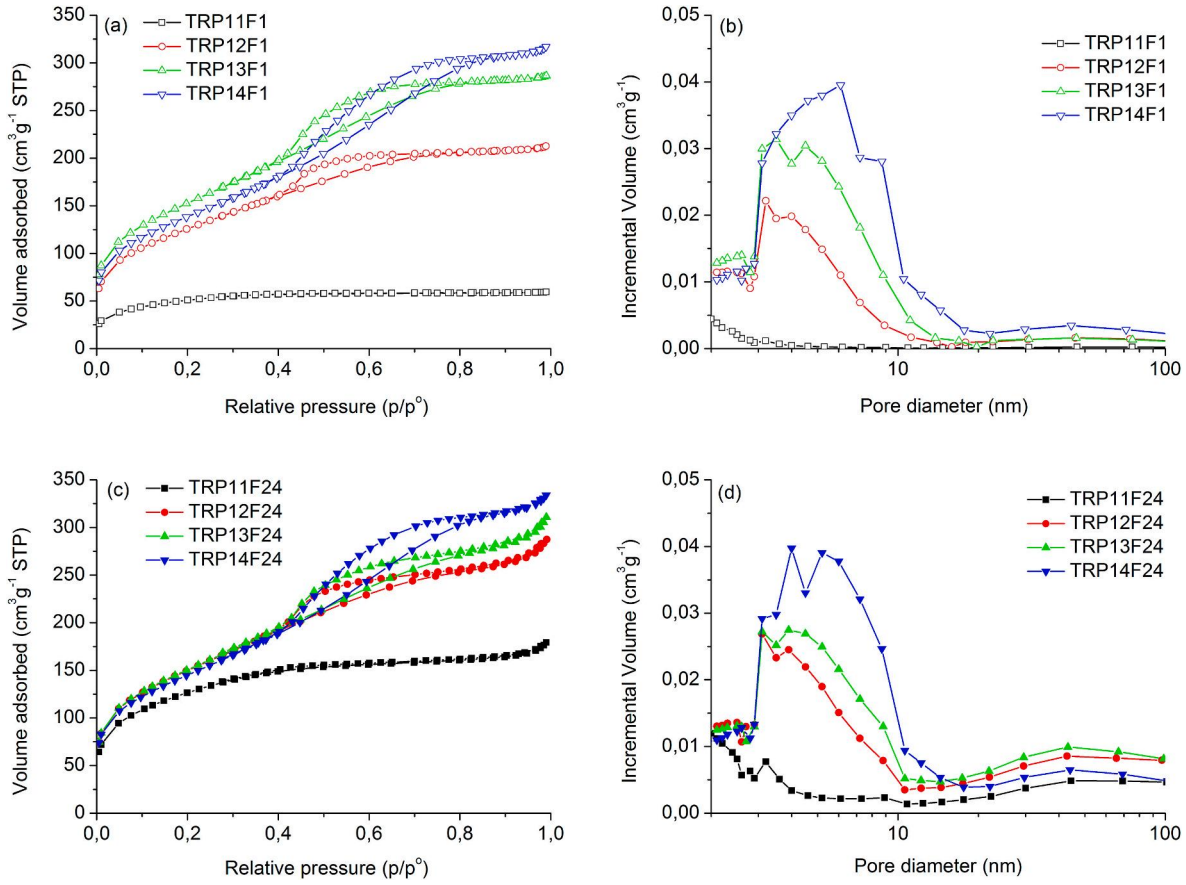

Fig. 5. N_2 adsorption-desorption isotherms (a, c) and PSDs (b, d) of SiOC-DC materials after HF etching during 1 or 24 h.

particles and smaller aggregates. As the pyrolysis temperature or etching time increase the particle size is progressively reduced, increasing the amount of aggregates, being especially noticeable when TRP11F1 and TRP14F24 are compared, as a consequence of a lesser or greater extraction of silica nano-domains, respectively (Fig. 6 (a),(d)). Those images are in consonance with the elemental chemical analysis (Table 1), FT-IR (Fig. 1), and XRD results (Fig. 2). There are many cracks located over the surface of particles, especially noticeable in bigger particles, which can appear due to the strain relaxation of SiOC during the extraction of silica nano-domains according to Raman results (Fig. 4). The presence of these cracks could be also associated with the beginning of silica extraction and therefore, with the formation of micropores, as it is supported by the N_2 adsorption-desorption data (Fig. 5, Table 5). In addition, as the silica extraction progresses the largest amount of agglomerates could be associated with a greater generation of mesopores. The images with the highest magnification (see insets of Fig. 6) unambiguously show the presence of a slit-like porous microstructure for the SiOC-CD material, previously assigned by N_2 adsorption/desorption measurements. The channels formed during etching time are bigger, wider and more abundant as pyrolysis temperature and/or time of etching increase which perfectly agree with N_2 adsorption-desorption data (Fig. 5, Table 5).

Table 5
Porosity data of SiOC-DC materials pyrolyzed at different temperatures after HF etching during 1 or 24 h.

Sample	*SSA* (m^2g^{-1})	S_{meso} (m^2g^{-1})	S_{micro} (m^2g^{-1})	V_{meso} (cm^3g^{-1})	V_{micro} (cm^3g^{-1})	D_{meso} (nm)
TRP11F1	182	62	119	0.04	0.06	2.3
TRP12F1	459	314	134	0.24	0.09	3.0
TRP13F1	556	419	124	0.35	0.10	3.3
TRP14F1	504	425	26	0.42	0.07	3.9
TRP11F24	454	206	228	0.15	0.12	3.0
TRP12F24	546	353	150	0.32	0.12	3.7
TRP13F24	549	372	121	0.37	0.11	3.9
TRP14F24	527	441	18	0.44	0.08	4.0

3.3. Electrochemical performance

3.3.1. Electrochemical characterisation and assessment

It is well known that apart from composition and functionalization *(i.e.,* O and F among others) of carbon based materials, the microstructure (*i.e.,* size and amount of pores) is determinant in order to achieve a good electrochemical response. The electrical conductivity can be increased with both the amount of carbon and the pyrolysis temperature of SiOC [13]. In addition, several studies point out that the O functionalities increase the wettability of the electrolyte leading to an effective mass transfer [14,16]. Besides, F functionalities increase the energy storage properties in carbon derived materials [55] since F carries a charge, creating electroactive sites for effective charge accumulation [62]. Furthermore, for supercapacitor applications it was initially believed that the presence of micropores in carbon materials, with high surface area, was enough in order to reach high theoretical C_s values [22]. However, recent studies indicate that narrow and large domains of micropores cannot put in contact the electrolyte and the surface reducing the C_s values, especially at high current loads [15]. In order to solve this problem, some new carbon derived materials include the presence of meso and also macropores that can act as pathways, enhancing the ion transportation improving the accessibility to micropores and then increasing the C_s, P_d and E_d values [10,12,15,63]. *A priori*, according with these requirements the most promising F-doped SiOC-DC materials for advanced electrochemical capacitors are those SiOC-DC materials pyrolyzed at the highest temperatures (*i.e.,* 1300–1400 °C) and then etched during 24 h. In order to confirm this hypothesis, the electrochemical characterization was performed over the F-doped SiOC-DC materials.

The CV curves are depicted in Fig. 7, Figure SI6 and Figure SI7. Independently of the etching time (*i.e.,* 1 (Figure SI6) or 24 h (Fig. 7), the SiOC-DC materials pyrolyzed at 1100 and 1200 °C display CV curves with a perfect rectangular shape characteristic of an electrochemical double layer capacitance behavior. The rectangular shape is maintained up to 1000 mVs^{-1} indicating the rapid formation of a double layer even at high rates (Figure SI7). In the case of the SiOC-DC materials pyrolyzed at 1300 and 1400 °C (Fig. 7 and Figure SI6), the CV rectangular shape is slightly distorted probably ascribed to a pseudocapacitive behavior [64] due to the contribution of surface redox reactions attributed to the presence of O and F functionalities. As it can be clearly observed, the area of the CV curves, directly related with C_s values, increases with the scan rate, the pyrolysis temperature and also with etching time (Fig. 7, Figure SI6 and Figure SI7). In the case of the samples etched during 24 h a great response of 30–50 Ag^{-1} is observed in the current-voltage curve at 1000 mVs^{-1}. This response increases with the pyrolysis temperature being the highest for the sample TRP13F24. The presence of a hierarchical porous microstructure with micro, meso and macropores together with the presence of O and F functionalities can explain the great electrochemical response of F-doped SiOC-DC materials.

As it is well-known, the EIS technique is a nondestructive tool, very useful to characterize the kinetic parameters. The typical *Nyquist* plots

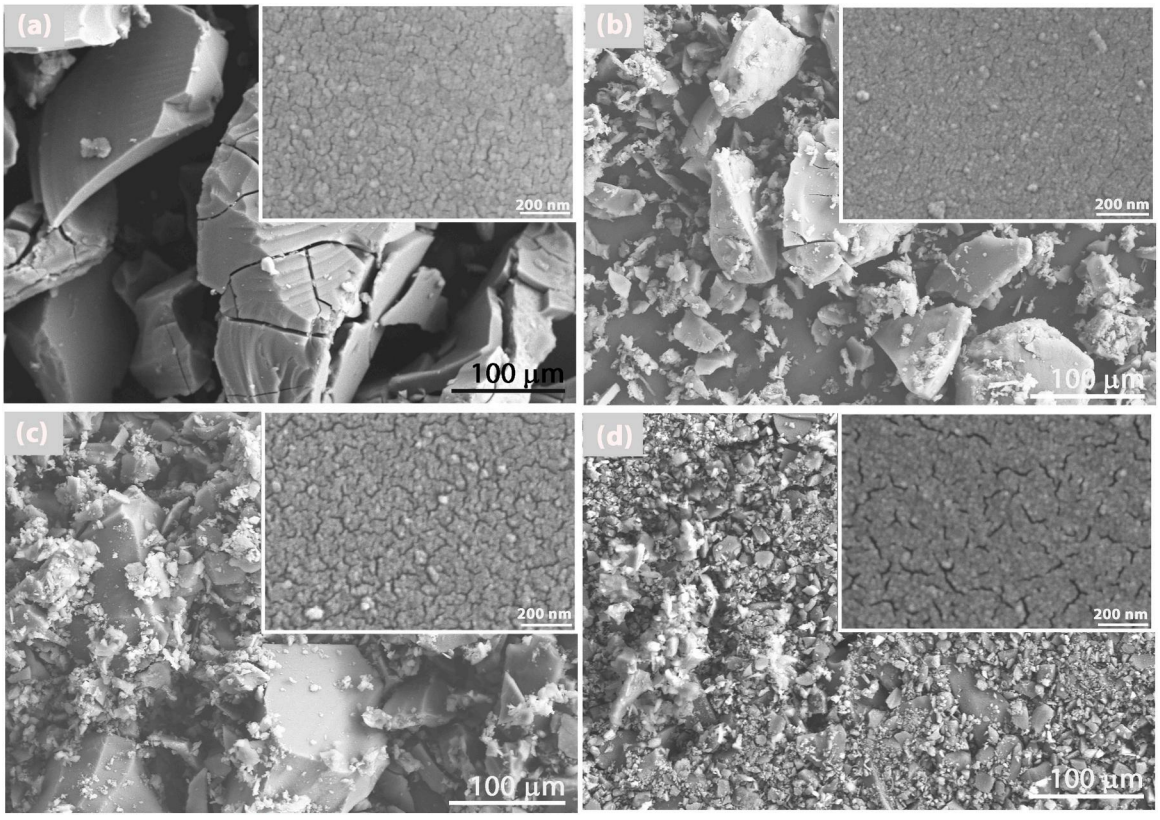

Fig. 6. FE-SEM micrographs of F-doped SiOC-DC materials pyrolyzed and etched under different conditions: (a) TRP11F1, (b) TRP11F24, (c) TRP14F1 and (d) TRP14F24, respectively.

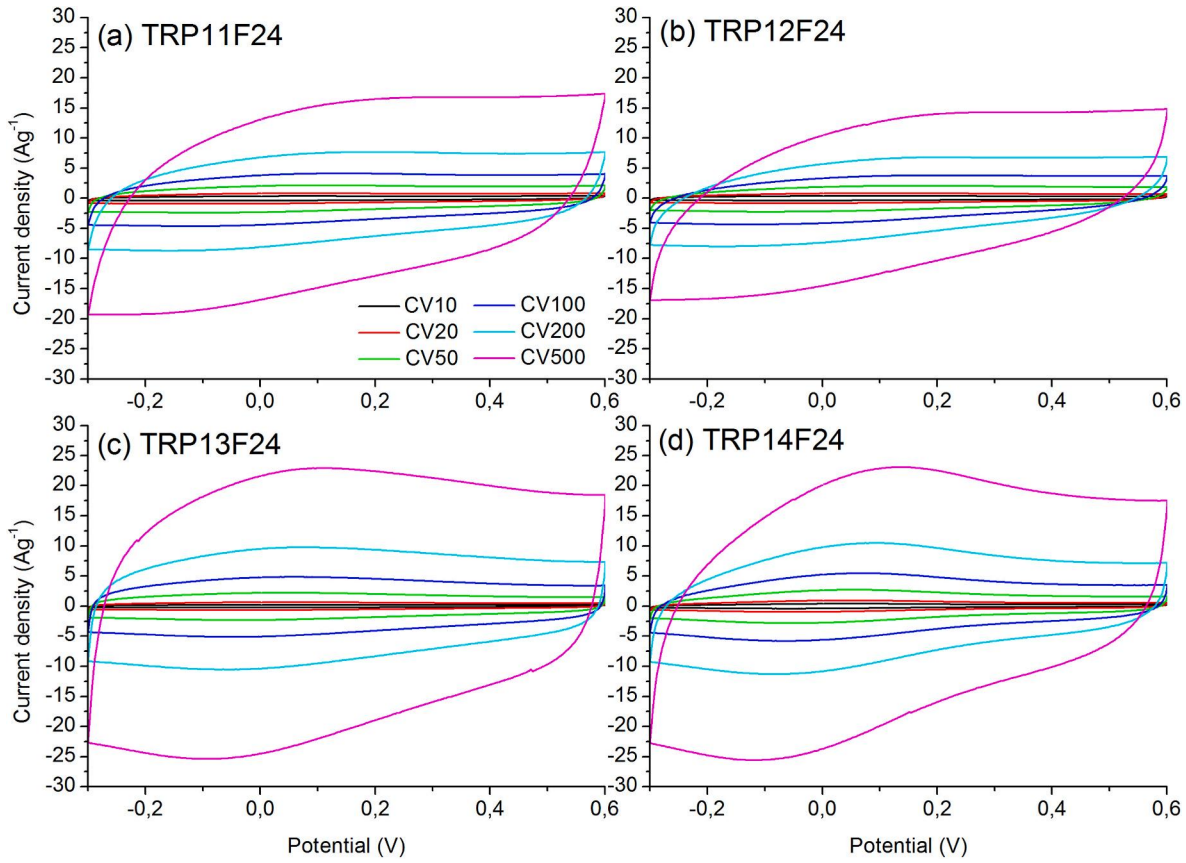

Fig. 7. CV curves at 10, 20, 50, 100, 200 and 500 $mVs^{-1}$of F-doped-SiO-DC materials etched during 24 h.

composed by a semicircle at high frequencies and an almost vertical line at low frequencies are collected in Fig. 8 (a) and (b). The intersection of the arc at higer frequencies corresponds to the equivalent series resistance (R_{ES}) related to the internal resistance of electrode and electrolyte, the diameter of the semicircle represents the charge transfer resistance (R_{CT}) at the electrode/electrolyte interface and the slope of the line corresponds to the capacitive behaviour and ion diffusion resistance in the samples [65].

In the case of F-doped SiOC-DC samples etched during 1 h, R_{ES} values are low except for the TRP11F1 sample, while in the case of those materials etched during 24 h, the values are low and rather similar independently of the pyrolysis temperature. R_{CT} decreases with the pyrolysis temperature and, in the case of samples pyrolyzed at 1100 °C the highest values can be somehow related to the lower mobility of the electrolyte within micropores of the electrode [27]. As the pyrolysis temperature increases the R_{CT} values decrease problably ascribed to the formation of the hierarchical porous microstructure composed by micro, meso and macropores and a lower resistance of electrolyte within the pores of the electrode [3]. In addition, the contribution of O and F funtionalities, which are more abundant as the temperature of pyrolysis and etching time increase, that enhances the wettability of the electrode and the accessibility of the pores to the electrolyte can not be ruled out. These funtionalities increase the contact area of the electrode and electrolyte offering favorable paths for the penetration and transportation of ions leading to a fast adsorption and diffusion of ions over the electrode surface [17].

Finally, for all the samples the almost vertical line at low frequencies indicates a typical capacitive behaviour associated to the high accessibility of the electrolyte within the hierarchically porous microstructure and a fast ion response [10]. Those lines are steeper as the pyrolysis temperature increases up to 1300 °C indicating a higher reactivity and faster reaction kinetics at this temperature. The *Ragone* plots are collected in Fig. 8 (c) and (d). The very high values near 90° indicate the ideal capacitive behavior of the samples. The phase angle increases with the pyrolysis temperature up to 1300 °C and is also slightly higher for the samples etched during 24 h. In all cases, these angles are $\leq$ 85 ° problably ascribed to the contribution of some pseudocapacitive process related to O and F funtionalities [66] which is in accordance with the CV results. The frequency at $\approx$ 45 ° is employed to calculate the time constant ($\tau_o = 1/f_o$) (Table 6) which is very low in all cases except for TRP11F24.

The GCD curves at 2 Ag^{-1} of the SiOC-DC materials etched during 1 or 24 h are collected in Fig. 9 (a) and (b), respectively. The almost symmetrical triangular profiles confirm the typical double layer capacitive properties. Fig. 9 (c) and (d) collect the GCD curves at different current densities of TRP14F1 and TRP14F24, respectively. The high retention ratios as the current increase imply a good rate capacity of the SiOC-DC porous materials. The C_s values of the F-doped SiOC-DC etched during 1 or 24 h are represented in Fig. 9 (e) and (f), respectively. In accordance with both the CV and EIS results, the C_s values increase with both the etching time and pyrolysis temperature. The highest values are obtained for the TRP13F24 and TRP14F24 samples which display rather similar C_s values. At 0.1 Ag^{-1} the materials display a C_s value of $\approx$ 225 Fg^{-1}, these values decrease as the current density increases, reaching C_s values of $\approx$ 200 Fg^{-1} at 2 Ag^{-1} and $\approx$ 165 Fg^{-1} at a very high current density of 30 Ag^{-1}. Slightly lower results have been obtained by SiOC-DC materials obtained by Cl_2 etching with very high *SSA* and C(%) [21,22,67]. On the contrary, comparable or higher values were obtained for SiOC-DC materials obtained after HF etching although those materials display much higher *SSA* and C(%) values [25,26].

3.3.2. *Textural, chemical features and electrochemical response relationships*

These C_s values can be partially explained by the hierarchical

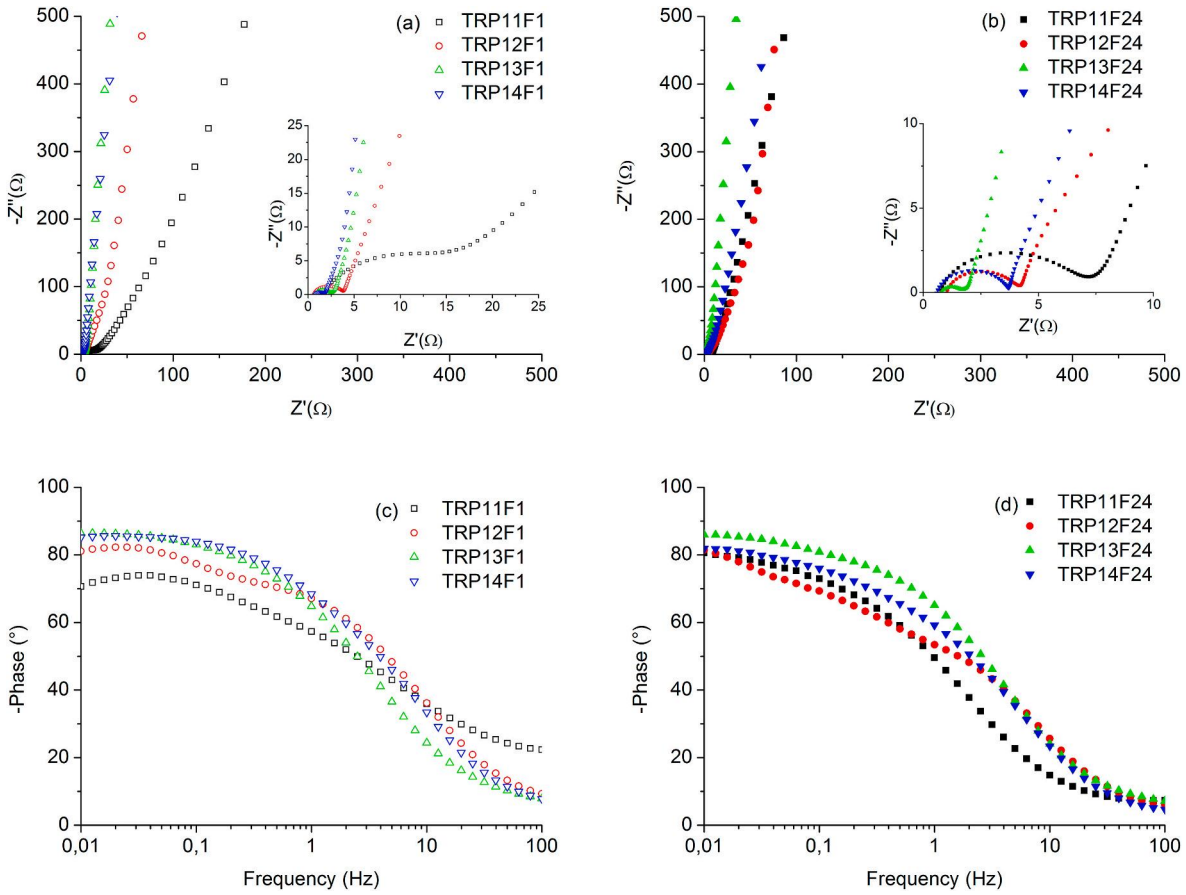

Fig. 8. Nyquist (a, b) and Ragone (c, d) plots of F-doped SiOC-DC etched during 1 or 24 h.

Table 6
R_{ES}, R_{CT}, f_o and τ_o values, extracted from EIS data, of F-doped SiOC-DC materials etched during 1 or 24 h.

	Etching time (h)	TRP11	TRP12	TRP13	TRP14
R_{ES} (Ω)	1	1.8	0.7	0.8	0.8
	24	0.8	1.0	0.8	0.6
R_{CT} (Ω)	1	12.8	3.2	1.7	1.0
	24	6.4	3.1	0.9	3.1
f_o (Hz)	1	4	6.3	3.2	5.0
	24	1.2	2.5	3.2	3.2
τ_o (s)	1	0.2	0.2	0.3	0.2
	24	0.8	0.4	0.3	0.3

microstructure where bigger pores (*i.e.,* macro and mesopores) create channels which facilitate the ions transportation to the lower pores (*i.e.,* micropores) [68]. The slit-like shape of the pores, deduced from N_2 adsorption-desorption analysis (Fig. 5) and FE-SEM micrographs (Fig. 6), is suitable for charge storage and release [25]. In this sense, for the etching time of 24 h, larger pores (i.e., channels), mesopores (3–10 nm) and also meso-macropores (≈ 50 nm) are developed from micropores (Fig. 5 (d), Table 5). In addition, the same trend is appreciated as the pyrolysis temperature increases, which explains the highest values reached for the TRP13F24 and TRP14F24 samples. However, these samples show great differences taking into account the microstructural parameters (TRP13F24: S_{meso} = 372 m^2g^{-1} S_{micro} = 121 m^2g^{-1} and TRP14F24: S_{meso} = 441 m^2g^{-1}, S_{micro} = 18 m^2g^{-1}, Table 5) pointing out that the presence of O and F functionalities cannot be ruled out. In this sense, fluorinated carbon materials were investigated as supercapacitors obtaining very promising results [66]. *Zhao* et al. [55] displayed C_S values of 100–105 Fg^{-1} (0.5 Ag^{-1}) for F-graphene derived from GO. *Bulusheva* et al. [62] showed C_s values of 80–158 Fg^{-1} (100–2 mVs^{-1}) for graphene derived from Br/F-graphite. *An* et al. [17] reported C_s values of 227-124 Fg^{-1} (1–100 Ag^{-1}) for F-graphene hydrogels obtained from GO.

Initially the HF etching produces the nucleophilic attack of F^- over polarized Si–O bonds producing the incorporation of fluorine into the SiOC network. As the etching time and the pyrolysis temperature increase the silica nano-domains are leached out, then the fluorine can be introduced into C_{free} phase noticeable by the presence of F–C doped bonds (both with semi-ionic and covalent C–F character). The presence of different types of F–C bonds must be determinant in the electrochemical response. In this sense, C–F semi-ionic bonds have superior electron conductivity and transport performance [65]. Besides, the presence of O containing groups increases the hydrophilicity of F-doped carbon materials [62] improving the wettability of the electrolyte inside the electrode and therefore, the electrochemical performance.

As it can be observed by FT-IR (Fig. 1 (b)) for the TRP14F24 sample when the pyrolysis temperature increases more inactive C–F covalent bonds and less O functionalities are formed. There are two phenomena which may explain why TRP13F24 and TRP14F24 with very different microstructures display rather similar values of C_s. First, the increase of C–F covalent bonds also produces the decrease of R_{CT} (Table 6) related to their lower conductivity [17]. Second, the decrease of O functionalities reduces the wettability of the electrode by the electrolyte reducing the reactivity as it is observed by the change of the slope of the line in the *Nyquist* plots (Fig. 8 (b)). This effect is attenuated in the case of the TRP14F24 sample, by the formation of larger, wider and more abundant channels of pores (meso (3–10 nm) and meso-macropores (≈ 50 nm) which facilitate the ion accessibility.

As it can be clearly observed from *Ragone* plots (Fig. 10), TRP13F24 and TRP14F24 display the highest values of energy densities. At low P_d of 0.1 $kWkg^{-1}$ these samples have an E_d of ≈ 28 $Whkg^{-1}$ while at 45 $kWkg^{-1}$ have an E_d ≈ 19 $Whkg^{-1}$. In the literature can be found higher

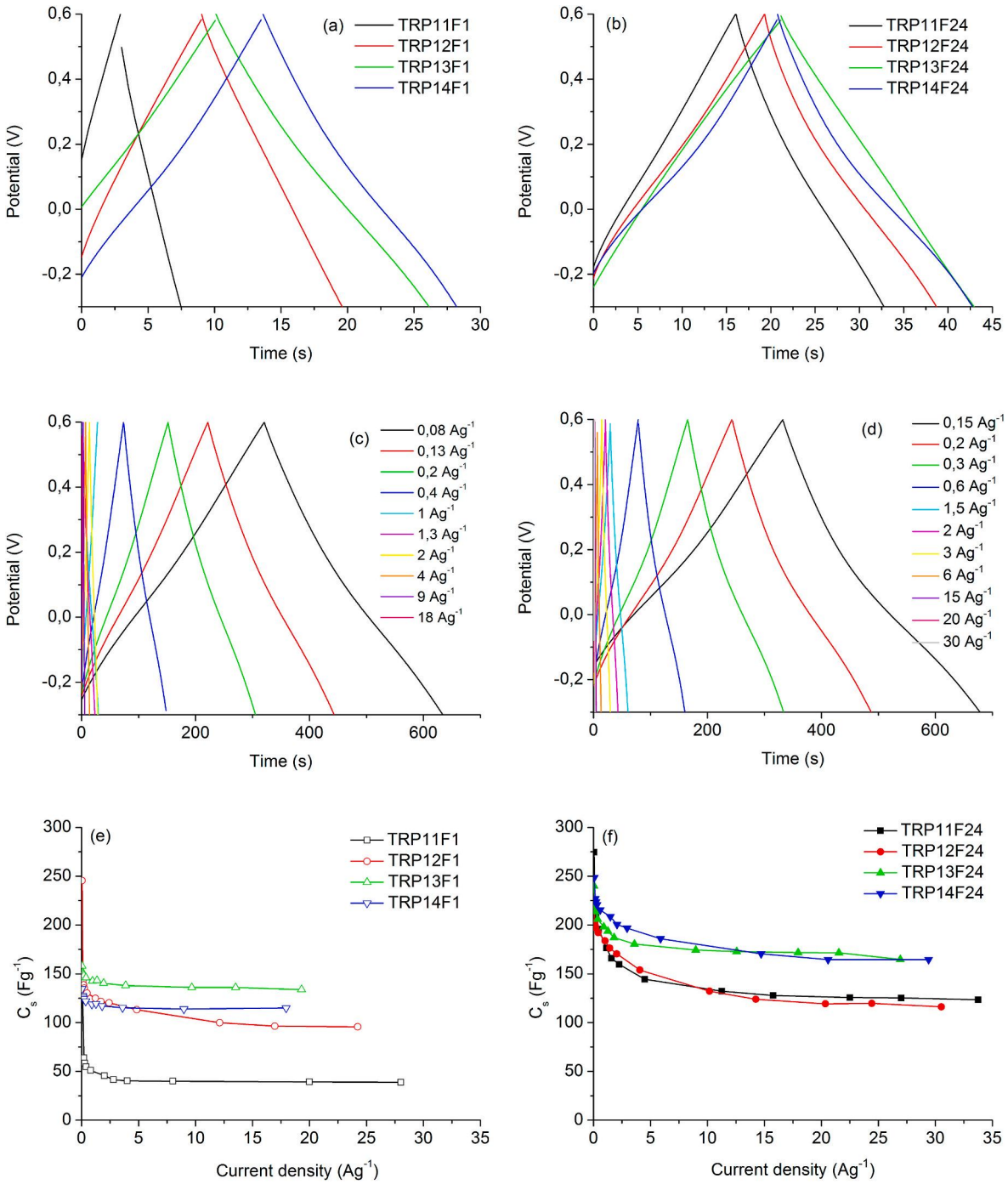

Fig. 9. GCD profiles at 2 Ag^{-1} of F-doped SiOC-DC samples etched during (a) 1 h or (b) 24 h; GCD profiles of (c) TRP14F1 and (d) TRP14F24 samples at different current densities; C_s values of SiOC-DC samples etched during (e) 1 or (f) 24 h.

or comparable values for SiOC-DC materials employing ionic liquids as electrolytes [10,21,23]. In this work, we have employed H_2SO_4 an inorganic aqueous electrolyte with an operational window of 0.9 V, much smaller than the ionic liquids ($\geq$ 2 V). It is obvious that as E_d varies with V^2 (eq. (3)), the values obtained with ionic liquids will be necessary higher than those obtained with inorganic aqueous electrolytes. This is why it is important to emphasize the results obtained in this work with a low operating window. Further work in this sense is now in progress.

4. Conclusions

Novel hierarchical micro-meso-macroporous fluorine-doped silicon oxycarbide derived carbon materials have been obtained by HF etching (1 or 24 h) at room temperature from silicon oxycarbides pyrolyzed at different temperatures ranged from 1100 to 1400 °C. The HF etching produces porous fluorine-doped silicon oxycarbide derived carbon materials with the formation of O and F functionalities under mild conditions.

At high temperatures, the phase separation promotes the silica etching and larger slit-like mesopores (3–10 nm) are created from micropores. For the longest etching time (24 h) wider meso-macropores (≈50 nm) are also obtained. The HF etching produces the grafting of fluorine in the silicon oxycarbide network (*i.e.,* SiO(F) bonds) but also into the free carbon phase with the formation of both C–F semi-ionic and

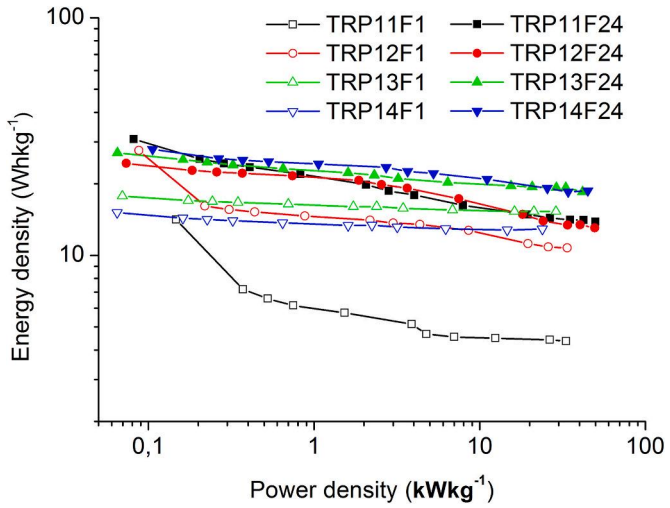

Fig. 10. Bode plots of F-doped SiOC-DC samples.

C–F covalent bonds. The formation of carbonyl groups is also determined.

The highest etching time and pyrolysis temperatures produce the enlargement of the created channels enhancing the ion accessibility, the mass diffusion pathways and the electrochemical response of the hierarchical materials. In addition, the formation of O and F functionalities promotes the wettability of the material generating electroactive sites and a pseudo-capacitance increasing the specific capacitance values. The materials etched during 24 h and pyrolyzed at 1300 or 1400 °C display a hierarchical porous microstructure composed by micro, meso and meso/macropores and also a large amount of F functionalities. All these facts produce the best electrochemical performance. The specific capacitance values vary from 225 to 156 Fg^{-1} (0.1–30 A g^{-1}) and energy density values vary from 28 to 19 $Whkg^{-1}$ at low and high power density values (0.1–45 $kWkg^{-1}$), respectively.

Finally, the fluorine-doped silicon oxycarbide derived carbon materials display a very interesting electrochemical performance, taking into account, the moderate values of specific surface area (≈ 550 m^2g^{-1}), amount of carbon (≈ 54(%)) and operating potential window (0.9 V) when are compared with related materials. Then, they can be potentially used as electrodes for supercapacitors in the field of energy storage applications. According to our results, we consider that TRP13F24 type-materials are the best for their industrial implementation since they are pyrolyzed at lower temperatures and display similar electrochemical values than those of TRP14F24. In addition, the raw materials are not too costly, and both the sol-gel process and the HF etching at room temperature could allow a relatively easy scaled up. However, before to do this implementation, further experiments about their stability during cycling are necessary to be done.

CRediT authorship contribution statement

M. Alejandra Mazo: Conceptualization, Writing – review & editing, Resources, Investigation, Methodology. **Maria T. Colomer:** Writing – review & editing, Resources, Funding acquisition. **Aitana Tamayo:** Funding acquisition, Resources. **Juan Rubio:** Writing – review & editing, Supervision, Resources, Investigation.

Declaration of competing interest

The authors declare that they have no known competing financial interests or personal relationships that could have appeared to influence the work reported in this paper.

Acknowledgements

This work was supported by project MAT2016-78700-R financed by Spanish Research Agency and European Regional Development Fund (AEI/FEDER, EU). The authors are also grateful to C. Díaz Dorado for her help with the revision of the figures. We acknowledge support of the publication fee by the CSIC Open Access Publication Support Initiative through its Unit of Information Resources for Research (URICI).

Appendix A. Supplementary data

Supplementary data to this article can be found online at https://doi.org/10.1016/j.micromeso.2021.111604.

References

[1] C. Vakifahmetoglu, V. Presser, S.H. Yeon, P. Colombo, Y. Gogotsi, Enhanced hydrogen and methane gas storage of silicon oxycarbide derived carbon, Microporous Mesoporous Mater. 144 (2011) 105–112, https://doi.org/10.1016/j.micromeso.2011.03.042.
[2] P.K. Chauhan, R. Parameshwaran, P. Kannan, R. Madhavaram, R. Sujith, Hydrogen storage in porous polymer derived Silicon Oxycarbide ceramics: outcomes and perspectives, Ceram. Int. 47 (2021) 2591–2599, https://doi.org/10.1016/j.ceramint.2020.09.105.
[3] L. Duan, Q. Ma, Z. Chen, Fabrication and CO_2 capture performance of silicon carbide derived carbons from polysiloxane, Microporous Mesoporous Mater. 203 (2015) 24–31, https://doi.org/10.1016/j.micromeso.2014.10.025.
[4] P. Moni, W.F. Chaves, M. Wilhelm, K. Rezwan, Polysiloxane microspheres encapsulated in carbon allotropes: a promising material for supercapacitor and carbon dioxide capture, J. Colloid Interface Sci. 542 (2019) 91–101, https://doi.org/10.1016/j.jcis.2019.01.087.
[5] K. Xia, X. Liu, H. Liu, Y. Lu, Z. Liu, Y. Li, L. Duan, Z. Hou, R. Li, D. Wang, Carbon-enriched SiOC ceramics with hierarchical porous structure as anodes for lithium storage, Electrochim. Acta 372 (2021) 137899, https://doi.org/10.1016/j.electacta.2021.137899.
[6] M. Weinberger, J. Munding, M. Lindén, M. Wohlfahrt-Mehrens, Template-derived submicrometric carbon spheres for lithium–sulfur and sodium-ion battery electrodes, Energy Technol. 6 (2018) 1797–1804, https://doi.org/10.1002/ENTE.201700932.
[7] C. Chandra, J. Kim, Silicon oxycarbide produced from silicone oil for high-performance anode material in sodium ion batteries, Chem. Eng. J. 338 (2018) 126–136, https://doi.org/10.1016/j.cej.2018.01.032.
[8] P. Moni, A. Deschamps, D. Schumacher, K. Rezwan, M. Wilhelm, A new silicon oxycarbide based gas diffusion layer for zinc-air batteries, J. Colloid Interface Sci. 577 (2020) 494–502, https://doi.org/10.1016/j.jcis.2020.05.041.
[9] M. Rose, Y. Korenblit, E. Kockrick, L. Borchardt, M. Oschatz, S. Kaskel, G. Yushin, Hierarchical micro- and mesoporous carbide-derived carbon as a high-performance electrode material in supercapacitors, Small 7 (2011) 1108–1117, https://doi.org/10.1002/smll.201001898.
[10] J. Yang, H. Wu, M. Zhu, W. Ren, Y. Lin, H. Chen, F. Pan, Optimized mesopores enabling enhanced rate performance in novel ultrahigh surface area meso-/microporous carbon for supercapacitors, Nano Energy 33 (2017) 453–461, https://doi.org/10.1016/j.nanoen.2017.02.007.
[11] J. Liu, L. Ma, Y. Zhao, H. Pan, H. Tang, H. Zhang, Porous structural effect of carbon electrode formed through one-pot strategy on performance of ionic liquid-based supercapacitors, Chem. Eng. J. 411 (2021) 128573, https://doi.org/10.1016/j.cej.2021.128573.
[12] C. Ma, Q. Fan, M. Dirican, N. Subjalearndee, H. Cheng, J. Li, Y. Song, J. Shi, X. Zhang, Rational design of meso-/micro-pores for enhancing ion transportation in highly-porous carbon nanofibers used as electrode for supercapacitors, Appl. Surf. Sci. 545 (2021) 148933, https://doi.org/10.1016/j.apsusc.2021.148933.
[13] J. Cordelair, P. Greil, Electrical conductivity measurements as a microprobe for structure transitions in polysiloxane derived Si-O-C ceramics, J. Eur. Ceram. Soc. 20 (2000) 1947–1957, https://doi.org/10.1016/S0955-2219(00)00068-6.
[14] Q. Li, R. Jiang, Y. Dou, Z. Wu, T. Huang, D. Feng, J. Yang, A. Yu, D. Zhao, Synthesis of mesoporous carbon spheres with a hierarchical pore structure for the electrochemical double-layer capacitor, Carbon N. Y. 49 (2011) 1248–1257, https://doi.org/10.1016/j.carbon.2010.11.043.
[15] W. Chen, X. Wang, C. Liu, M. Luo, P. Yang, X. Zhou, Rapid single-step synthesis of porous carbon from an agricultural waste for energy storage application, Waste Manag. 102 (2020) 330–339, https://doi.org/10.1016/j.wasman.2019.10.058.
[16] M. Kim, I. Oh, J. Kim, Influence of surface oxygen functional group on the electrochemical behavior of porous silicon carbide based supercapacitor electrode, Electrochim. Acta 196 (2016) 357–368, https://doi.org/10.1016/j.electacta.2016.03.021.
[17] H. An, Y. Li, P. Long, Y. Gao, C. Qin, C. Cao, Y. Feng, W. Feng, Hydrothermal preparation of fluorinated graphene hydrogel for high-performance supercapacitors, J. Power Sources 312 (2016) 146–155, https://doi.org/10.1016/j.jpowsour.2016.02.057.
[18] X. Zhang, X. Wang, L. Jiang, H. Wu, C. Wu, J. Su, Effect of aqueous electrolytes on the electrochemical behaviors of supercapacitors based on hierarchically porous

carbons, J. Power Sources 216 (2012) 290–296, https://doi.org/10.1016/j.jpowsour.2012.05.090.
[19] K. Lu, Porous and high surface area silicon oxycarbide-based materials - a review, Mater. Sci. Eng. R Rep. 97 (2015) 23–49, https://doi.org/10.1016/j.mser.2015.09.001.
[20] C. Vakifahmetoglu, D. Zeydanli, P. Colombo, Porous polymer derived ceramics, Mater. Sci. Eng. R Rep. 106 (2016) 1–30, https://doi.org/10.1016/j.mser.2016.05.001.
[21] A. Meier, M. Weinberger, K. Pinkert, M. Oschatz, S. Paasch, L. Giebeler, H. Althues, E. Brunner, J. Eckert, S. Kaskel, Silicon oxycarbide-derived carbons from a polyphenylsilsequioxane precursor for supercapacitor applications, Microporous Mesoporous Mater. 188 (2014) 140–148, https://doi.org/10.1016/j.micromeso.2013.12.022.
[22] L. Duan, Q. Ma, L. Mei, Z. Chen, Fabrication and electrochemical performance of nanoporous carbon derived from silicon oxycarbide, Microporous Mesoporous Mater. 202 (2015) 97–105, https://doi.org/10.1016/j.micromeso.2014.09.047.
[23] B. Krüner, C. Odenwald, A. Tolosa, A. Schreiber, M. Aslan, G. Kickelbick, V. Presser, Carbide-derived carbon beads with tunable nanopores from continuously produced polysilsesquioxanes for supercapacitor electrodes, Sustain. Energy Fuels 1 (2017) 1588–1600, https://doi.org/10.1039/c7se00265c.
[24] M.A. Mazo, A. Tamayo, J. Rubio, Highly micro- and mesoporous oxycarbide derived materials from HF etching of silicon oxycarbide materials, Microporous Mesoporous Mater. 289 (2019) 109614, https://doi.org/10.1016/j.micromeso.2019.109614.
[25] I.P. Swain, S. Pati, S.K. Behera, A preceramic polymer derived nanoporous carbon hybrid for supercapacitors, Chem. Commun. 55 (2019) 8631–8634, https://doi.org/10.1039/c9cc04146j.
[26] I.P. Swain, S.K. Behera, Nanoporous carbon hybrids derived from polymethylsilsequioxane for ultracapacitor electrodes, Microporous Mesoporous Mater. 303 (2020) 110290, https://doi.org/10.1016/j.micromeso.2020.110290.
[27] M.A. Mazo, M.T. Colomer, A. Tamayo, J. Rubio, Microstructure-electrochemical behavior relationships of hierarchically micro-mesoporous silicon oxycarbide derived materials obtained by the pyrolysis of trietoxysilane/dimethyldiphenylsiloxane hybrids, J. Alloys Compd. 870 (2021) 159427, https://doi.org/10.1016/j.jallcom.2021.159427.
[28] H. Sun, J. Pan, X. Yan, W. Shen, W. Zhong, X. Cheng, MnO_2 nanoneedles loaded on silicon oxycarbide-derived hierarchically porous carbon for supercapacitor electrodes with enhanced electrochemical performance, Ceram. Int. 45 (2019) 24802–24810, https://doi.org/10.1016/j.ceramint.2019.08.222.
[29] J. Pan, H. Sun, X. Yan, W. Zhong, W. Shen, Y. Zhang, X. Cheng, Cube Fe_3O_4 nanoparticles embedded in three-dimensional net porous carbon from silicon oxycarbide for high performance supercapacitor, Ceram. Int. 46 (2020) 24805–24815, https://doi.org/10.1016/j.ceramint.2020.05.098.
[30] R.K. Iler, The Chemistry of Silica: Solubility, Polymerization, Colloid and Surface Properties and Biochemistry of Silica, John Wiley and Sons Inc, New York, 1979. http://ci.nii.ac.jp/naid/10029819198/en/.
[31] G.D. Sorarù, S. Modena, E. Guadagnino, P. Colombo, J. Egan, C. Pantano, Chemical durability of silicon oxycarbide glasses, J. Am. Ceram. Soc. 85 (2002) 1529–1536, https://doi.org/10.1111/j.1151-2916.2002.tb00308.x.
[32] R. Peña-Alonso, G. Mariotto, C. Gervais, F. Babonneau, G.D. Soraru, New insights on the high-temperature nanostructure evolution of SiOC and B-doped SiBOC polymer-derived glasses, Chem. Mater. 19 (2007) 5694–5702, https://doi.org/10.1021/cm071203q.
[33] M.F. Iastrenski, P.R. Catarini da Silva, C.R. Teixeira Tarley, M.G. Segatelli, Influence of molecular architecture of Si-containing precursors and HF chemical treatment on structural and textural features of silicon oxycarbide (SiOC) materials, Ceram. Int. 45 (2019) 21698–21708, https://doi.org/10.1016/j.ceramint.2019.07.170.
[34] M.A. Mazo, A. Tamayo, J. Rubio, Stable highly porous silicon oxycarbide glasses from pre-ceramic hybrids, J. Mater. Chem. 3 (2015) 23220–23229, https://doi.org/10.1039/c5ta05656j.
[35] C.G. Pantano, A.K. Singh, H. Zhang, Silicon oxycarbide glasses, J. Sol. Gel Sci. Technol. 14 (1999) 7–25, https://doi.org/10.1023/A:1008765829012.
[36] R. Peña-Alonso, G.D. Sorarù, R. Raj, Preparation of ultrathin-walled carbon-based nanoporous structures by etching pseudo-amorphous silicon oxycarbide ceramics, J. Am. Ceram. Soc. 89 (2006) 2473–2480, https://doi.org/10.1111/j.1551-2916.2006.01117.x.
[37] G.D. Sorarù, R. Pena-Alonso, M. Leoni, C-rich micro/mesoporous Si(B)OC: in situ diffraction analysis of the HF etching process, Microporous Mesoporous Mater. 172 (2013) 125–130, https://doi.org/10.1016/j.micromeso.2013.01.026.
[38] A.M. Wilson, G. Zank, K. Eguchi, W. Xing, B. Yates, J.R. Dahn, Pore creation in silicon oxycarbides by rinsing in dilute hydrofluoric acid, Chem. Mater. 9 (1997) 2139–2144, https://doi.org/10.1021/cm970224p.
[39] G.D. Sorarù, G. D'Andrea, R. Campostrini, F. Babonneau, G. Mariotto, Structural characterization and high-temperature behavior of silicon oxycarbide glasses prepared from sol-gel precursors containing Si-H bonds, J. Am. Ceram. Soc. 78 (1995) 379–387, https://doi.org/10.1111/j.1151-2916.1995.tb08811.x.
[40] S. Brunauer, P.H. Emmett, E. Teller, Adsorption of gases in multimolecular layers, J. Am. Chem. Soc. 60 (1938) 309–319, https://doi.org/10.1021/ja01269a023.
[41] E.P. Barrett, L.G. Joyner, P.P. Halenda, The determination of pore volume and area distributions in porous substances. I. Computations from nitrogen isotherms, J. Am. Chem. Soc. 73 (1951) 373–380, https://doi.org/10.1021/JA01145A126.
[42] S. Zhang, N. Pan, Supercapacitors performance evaluation, Adv. Energy Mater. 5 (2015) 1401401, https://doi.org/10.1002/AENM.201401401.
[43] J.L. Oteo, M.A. Mazo, C. Palencia, F. Rubio, J. Rubio, Synthesis and characterization of silicon oxycarbide derived nanocomposites obtained through ceramic processing of TEOS/PDMS preceramic materials, J. Nano Res. 14 (2011) 27–38. https://doi.org/10.4028/www.scientific.net/JNanoR.14.27.
[44] C. Vix-Guterl, I. Alix, P. Gibot, P. Ehrburger, Formation of tubular silicon carbide from a carbon-silica material by using a reactive replica technique: infra-red characterisation, Appl. Surf. Sci. 210 (2003) 329–337, https://doi.org/10.1016/S0169-4332(03)00147-8.
[45] M.A. Mazo, A. Tamayo, J. Rubio, Advanced silicon oxycarbide-carbon composites for high temperature resistant friction systems, J. Eur. Ceram. Soc. 36 (2016) 2443–2452, https://doi.org/10.1016/j.jeurceramsoc.2016.03.012.
[46] D. Assefa, E. Zera, R. Campostrini, G.D. Soraru, C. Vakifahmetoglu, Polymer-derived SiOC aerogel with hierarchical porosity through HF etching, Ceram. Int. 42 (2016) 11805–11809, https://doi.org/10.1016/j.ceramint.2016.04.101.
[47] F. Kolář, V. Machovič, J. Svítilová, L. Borecká, Structural characterization and thermal oxidation resistance of silicon oxycarbides produced by polysiloxane pyrolysis, Mater. Chem. Phys. 86 (2004) 88–98, https://doi.org/10.1016/j.matchemphys.2004.02.011.
[48] M. Kanezashi, T. Matsutani, T. Wakihara, H. Nagasawa, T. Okubo, T. Tsuru, Preparation and gas permeation properties of fluorine-silica membranes with controlled amorphous silica structures: effect of fluorine source and calcination temperature on network size, ACS Appl. Mater. Interfaces 9 (2017) 24625–24633, https://doi.org/10.1021/acsami.7b06800.
[49] Y. Wang, W.C. Lee, K.K. Manga, P.K. Ang, J. Lu, Y.P. Liu, C.T. Lim, K.P. Loh, Fluorinated graphene for promoting neuro-induction of stem cells, Adv. Mater. 24 (2012) 4285–4290, https://doi.org/10.1002/adma.201200846.
[50] C.J. Fang, L. Ley, H.R. Shanks, K.J. Gruntz, M. Cardona, Bonding of fluorine in amorphous hydrogenated silicon, Phys. Rev. B 22 (1980) 6140–6148, https://doi.org/10.1103/PhysRevB.22.6140.
[51] S.M. Lyth, W. Ma, J. Liu, T. Daio, K. Sasaki, A. Takahara, B. Ameduri, Solvothermal synthesis of superhydrophobic hollow carbon nanoparticles from a fluorinated alcohol, Nanoscale 7 (2015) 16087, https://doi.org/10.1039/c5nr03484a.
[52] L.A. Zazzera, J.F. Moulder, XPS and SIMS study of anhydrous HF and UV/Ozone-Modified Silicon (100) surfaces, J. Electrochem. Soc. 136 (1989) 484–491, https://doi.org/10.1149/1.2096659.
[53] D. Briggs, D. Wanger, W.M. Riggs, L.E. Davis, J.F. Moulder, G.E. Muilenberg Perkin-Elmer, Handbook of X-Ray Photoelectron Spectroscopy C, Corp., Physical Electronics Division, Eden Prairie, Minnesota, USA, 1979, pp. 190–195. , Surf. Interface Anal. 3 (1981).
[54] G.D. Sorarù, G. D'Andrea, A. Glisenti, XPS characterization of gel-derived silicon oxycarbide glasses, Mater. Lett. 27 (1996) 1–5, https://doi.org/10.1016/0167-577X(95)00245-6.
[55] F.G. Zhao, G. Zhao, X.H. Liu, C.W. Ge, J.T. Wang, B.L. Li, Q.G. Wang, W.S. Li, Q. Y. Chen, Fluorinated graphene: facile solution preparation and tailorable properties by fluorine-content tuning, J. Mater. Chem. A. 2 (2014) 8782–8789, https://doi.org/10.1039/c4ta00847b.
[56] F. Tuinstra, J.L. Koenig, Raman spectrum of graphite, Cit. J. Chem. Phys. 53 (1970) 1126–1130, https://doi.org/10.1063/1.1674108.
[57] A. Ferrari, J. Robertson, Interpretation of Raman spectra of disordered and amorphous carbon, Phys. Rev. B Condens. Matter 61 (2000) 14095–14107, https://doi.org/10.1103/PhysRevB.61.14095.
[58] A.C. Ferrari, J.C. Meyer, V. Scardaci, C. Casiraghi, M. Lazzeri, F. Mauri, S. Piscanec, D. Jiang, K.S. Novoselov, S. Roth, A.K. Geim, Raman spectrum of graphene and graphene layers, Phys. Rev. Lett. 97 (2006) 187401, https://doi.org/10.1103/PhysRevLett.97.187401, 1–4.
[59] P. Lespade, A. Marchand, M. Couzi, F. Cruege, Caracterisation de materiaux carbones par microspectrometrie Raman, Carbon N. Y. 22 (1984) 375–385, https://doi.org/10.1016/0008-6223(84)90009-5.
[60] D.S. Knight, W.B. White, Characterization of diamond films by Raman spectroscopy, J. Mater. Res. 4 (1989) 385–393, https://doi.org/10.1557/JMR.1989.0385.
[61] M. Thommes, K. Kaneko, A. V Neimark, J.P. Olivier, F. Rodriguez-Reinoso, J. Rouquerol, K.S.W. Sing, IUPAC Technical Report Physisorption of gases, with special reference to the evaluation of surface area and pore size distribution (IUPAC Technical Report), Pure Appl. Chem. 87 (2015) 1051–1069, https://doi.org/10.1515/pac-2014-1117.
[62] L.G. Bulusheva, V.A. Tur, E.O. Fedorovskaya, I.P. Asanov, D. Pontiroli, M. Riccò, A. V. Okotrub, Structure and supercapacitor performance of graphene materials obtained from brominated and fluorinated graphites, Carbon N. Y. 78 (2014) 137–146, https://doi.org/10.1016/j.carbon.2014.06.061.
[63] H. Lim, H. Kim, S.O. Kim, K.J. Kim, W. Choi, Novel approach for controlling free-carbon domain in silicone oil-derived silicon oxycarbide (SiOC) as an anode material in secondary batteries, Chem. Eng. J. 404 (2021) 126581, https://doi.org/10.1016/j.cej.2020.126581.
[64] Y. Gogotsi, R.M. Penner, Energy storage in nanomaterials – capacitive, pseudocapacitive, or battery-like? ACS Nano 12 (2018) 2081–2083, https://doi.org/10.1021/ACSNANO.8B01914.
[65] W. Peng, H. Li, S. Song, Synthesis of fluorinated graphene/CoAl-layered double hydroxide composites as electrode materials for supercapacitors, ACS Appl. Mater. Interfaces 9 (2017) 5204–5212, https://doi.org/10.1021/acsami.6b11316.
[66] H. Jia, J. Zhu, M. Zhang, S. Sang, F. Hu, F. Zhang, Fluorine and nitrogen co-doped mesoporous carbon derived from polytetrafluoroethylene@melamine sponge for

supercapacitor application, J. Energy Storage 38 (2021) 102613, https://doi.org/10.1016/J.EST.2021.102613.
[67] A. Tolosa, B. Krüner, N. Jäckel, M. Aslan, C. Vakifahmetoglu, V. Presser, Electrospinning and electrospraying of silicon oxycarbide-derived nanoporous carbon for supercapacitor electrodes, J. Power Sources 313 (2016) 178–188, https://doi.org/10.1016/J.JPOWSOUR.2016.02.077.
[68] M. Sevilla, A.B. Fuertes, Direct synthesis of highly porous interconnected carbon nanosheets and their application as high-performance supercapacitors, ACS Nano 8 (2014) 5069–5078, https://doi.org/10.1021/NN501124H.